Evaluation of Carbon Partitioning in New Generation of Quench and Partitioning (Q&P) Steels

EDWAN ANDERSON ARIZA, JONATHAN POPLAWSKY, WEI GUO, KINGA UNOCIC, ANTONIO J. RAMIREZ, ANDRÉ P. TSCHIPTSCHIN, and SUDARSANAM SURESH BABU

Quenching and partitioning (Q&P) and a novel combined process of hot straining (HS) and Q&P (HSQ&P) treatments have been applied to a TRIP-assisted steel in a Gleeble®3S50 thermomechanical simulator. The heat treatments involved intercritical annealing at 800 °C and a two-step Q&P heat treatment with a partitioning time of 100 seconds at 400 °C. The "optimum" quench temperature of 318 °C was selected according to the constrained carbon equilibrium (CCE) criterion. The effects of high-temperature deformation (isothermal and non-isothermal) on the carbon enrichment of austenite, carbide formation, and the strain-induced transformation to ferrite (SIT) mechanism were investigated. Carbon partitioning from supersaturated martensite into austenite and carbide precipitation were confirmed by means of atom probe tomography (APT) and scanning transmission electron microscopy (STEM). Austenite carbon enrichment was clearly observed in all specimens, and in the HSQ&P samples, it was significantly greater than in Q&P, suggesting an additional carbon partitioning to austenite from ferrite formed by the deformation-induced austenite-to-ferrite transformation (DIFT) phenomenon. By APT, the carbon accumulation at austenite/martensite interfaces was observed, with higher values for HSQ&P deformed isothermally (≈ 11 at. pct), when compared with non-isothermal HSQ&P (≈ 9.45 at. pct) and Q&P (≈ 7.6 at. pct). Moreover, a local Mn enrichment was observed in a ferrite/austenite interface, indicating ferrite growth under local equilibrium with negligible partitioning (LENP).

EDWAN ANDERSON ARIZA is with the Department of Metallurgical and Materials Engineering, University of São Paulo, Av. Prof. Mello Moraes, 2463, São Paulo, SP, 05508-030, Brazil and also with the Mechanical Technology Program, Technological University of Pereira, Cra. 27 No. 10-02, Barrio Alamos, Pereira, Risaralda, Colombia. Contact e-mail: andersonariza@usp.br. JONATHAN POPLAWSKY and WEI GUO are with the Center for Nanophase Materials Sciences, Oak Ridge National Laboratory, P.O. Box 2008, Oak Ridge-TN 37831-6064. KINGA UNOCIC is with the Materials Science and Technology Division, Oak Ridge National Laboratory, P.O. Box 2008, Oak Ridge-TN 37831-6139. ANTONIO J. RAMIREZ is with the Department of Materials Science and Engineering, Ohio State University, Columbus-OH, 43221. ANDRÉ P. TSCHIPTSCHIN is with the Department of Metallurgical and Materials Engineering, University of São Paulo. SUDARSANAM SURESH BABU, is with the Department of Mechanical, Aerospace and Biomedical Engineering, The University of Tennessee, Knoxville-TN, 37996-2210.

I. INTRODUCTION

CARBON in retained austenite is considered to be the chemical element that controls its stability at room temperature and the plasticity of the material, especially in low-alloy steels.[1] However, in transformation-induced plasticity (TRIP) steels, research has shown that the stability of the retained austenite is affected not only by the carbon[2,3] or manganese content,[4,5] but also by its distribution, morphology, and grain size.[6,7] The constraints imposed by the phases surrounding the austenitic phase,[8] and the austenite crystallographic orientation, in relation to the loading direction (Schmid factor), also influences the stability of retained austenite.[9,10] With regard to the dependence of the austenite grain morphology on the carbon content of retained austenite, there is a notable discrepancy in the literature. Some authors report that austenite in the form of films has a higher carbon content,[11–13] while others assert the opposite, that austenite in the form of blocks has shown a higher carbon content.[14,15] However, all these authors concur that austenite retained in the form of films is more stable against mechanical deformation, even when having a lower carbon content. This behavior is mainly associated with the greater number of defects, such as stacking faults or dislocations, present in

austenite in the form of blocks,[12] which act as martensite nucleation sites, even at low deformations. Furthermore, interlath retained austenite films are generally surrounded by microconstituents with greater hardness and strength to plastic flow, such as martensite and bainite. Thus, the austenite is stabilized by the high hydrostatic pressure (up to 700 MPa[16]) exerted by these phases, which restricts the volumetric expansion and the shear strain associated with the martensitic transformation.[12,17] Hence, since the retained austenite's stability and the carbon distribution are assumed to be the key parameters that influence the phase transformations and mechanical properties, the characterization and understanding of carbon enrichment and the volume fraction of retained austenite are important.

The underlying principle of the "quenching and partitioning" (Q&P) process[18] is the transfer of carbon from the supersaturated martensite to the austenite. In the Q&P process, the fully or partially austenitized steel is rapidly cooled to a preconfigured quench temperature (T_Q), which is lower than the martensite start temperature (M_s) but higher than the martensite finish temperature (M_f), in order to form a microstructure consisting of a determined volume fraction of martensite, untransformed austenite, and intercritical ferrite (in the case of the initial intercritical annealing). The samples are then submitted to the partitioning step, holding the samples at the same (one-step Q&P) or at a slightly greater temperature than the initial T_Q (two step Q&P). At the quench temperature, the carbon content in martensite is the same as the bulk carbon content in samples that have been quenched from austenite. On the other hand, in intercritically annealed samples, the carbon content in martensite is greater than the bulk carbon content.[19] During a subsequent isothermal holding (partitioning stage), the carbon can diffuse from the supersaturated athermal martensite into the remaining untransformed austenite, thereby stabilizing austenite during the final quench to room temperature. It has been suggested that this carbon partitioning is controlled by the constrained carbon equilibrium (CCE) criterion,[20–22] which assumes an identical chemical potential of carbon (not applicable to substitutional solutes) in each phase, a stationary austenite/martensite interface, and that no competing reactions occur, such as carbide precipitation.

Carbon-enriched austenite stabilized at room temperature has the ability to contribute to mechanical properties in the same way that it does in TRIP-assisted steels.[23] Moreover, the enriched carbon concentration also increases the strength of the partitioned untransformed austenite.[24] For this reason, the subject of Q&P has been extensively studied during the past few years.[25–28] Liu et al.[29] indicated that while the Q&P process is one of the most likely methods for the production of AHSS with high strength and elongation, the heat treatment methods do not take into account the strain-induced phase transformations. Some studies have investigated the possibility of using a combination of the quenching and partitioning with the hot stamping process.[29–34] Furthermore, those studies only used isothermal straining and one-step Q&P condition in

samples fully austenitized, with the exception of Ariza et al.[34] and Chang et al.[31] However, Chang et al.[31] implemented a two-step Q&P process, with one minute of quenching time, before the partitioning treatment, which is a longer period of time than was suggested by De Knijf et al.,[35] since it can cause the precipitation of isothermal products.

Atom probe tomography (APT) has emerged as a unique technique that is able to provide information about the three-dimensional distribution of elements with nanoscale resolution. Some authors[19,27,36–38] carried out APT measurements to obtain information on the amount and location of carbon within Q&P microstructures. However, there is still not enough information on the carbon enrichment of austenite in the Q&P treatment after deformation at high temperatures (henceforth referred to as HSQ&P). Hence, the APT technique is able to clarify whether the DIFT (deformation-induced ferrite transformation) effect[39] or the strain-induced transformation to ferrite (SITF) mechanism[40] contributes to the enrichment of austenite and its stabilization and whether carbide precipitation concomitant with ferrite precipitation hinders the diffusion of carbon to neighboring austenite.

In this study, a novel combined process of hot straining, using an isothermal and a non-isothermal deformation and intercritical annealing, followed by a two-step Q&P treatment (HSQ&P) applied to TRIP-assisted steel, has been conducted. The aim is to compare the Q&P process with the same process when previous hot deformation is included. In order to understand the role of the partitioning stage on the distribution (or segregation) of the solute (carbon and substitutional elements) in the retained austenite, ferrite, martensite, and the tempering reactions that may occur (such as carbide precipitation or carbon atom clustering at the dislocations or at the interfaces), with a special focus on the carbon and manganese profiles, the samples were analyzed by APT in regions identified as austenite (both block and film), ferrite, martensite, interfaces, and carbides. The understanding of carbon redistribution during the Q&P and HSQ&P processes is important for the development of complex microstructures in advanced high-strength steels.

II. EXPERIMENTAL PROCEDURES

A commercial TRIP-assisted steel (Fe–0.23C–1.23-Si–1.50Mn, wt pct) was subjected to Q&P and HSQ&P experiments. A Gleeble®3S50 thermomechanical simulator was used to create the thermomechanical treatment conditions, as shown in Figure 1. The as-received TRIP-assisted steel samples were heated at a rate of 15 °C/s until they reached a temperature of 1000 °C, this temperature was maintained for 5 minutes in order to become homogeneous, and then the samples were intercritically annealed at 800 °C for 5 minutes. For the HSQ&P processes, after intercritical annealing, the samples were strained. The true strain was 30 pct and the initial straining temperatures were 750 °C (a non-isothermal process, where the sample is cooled
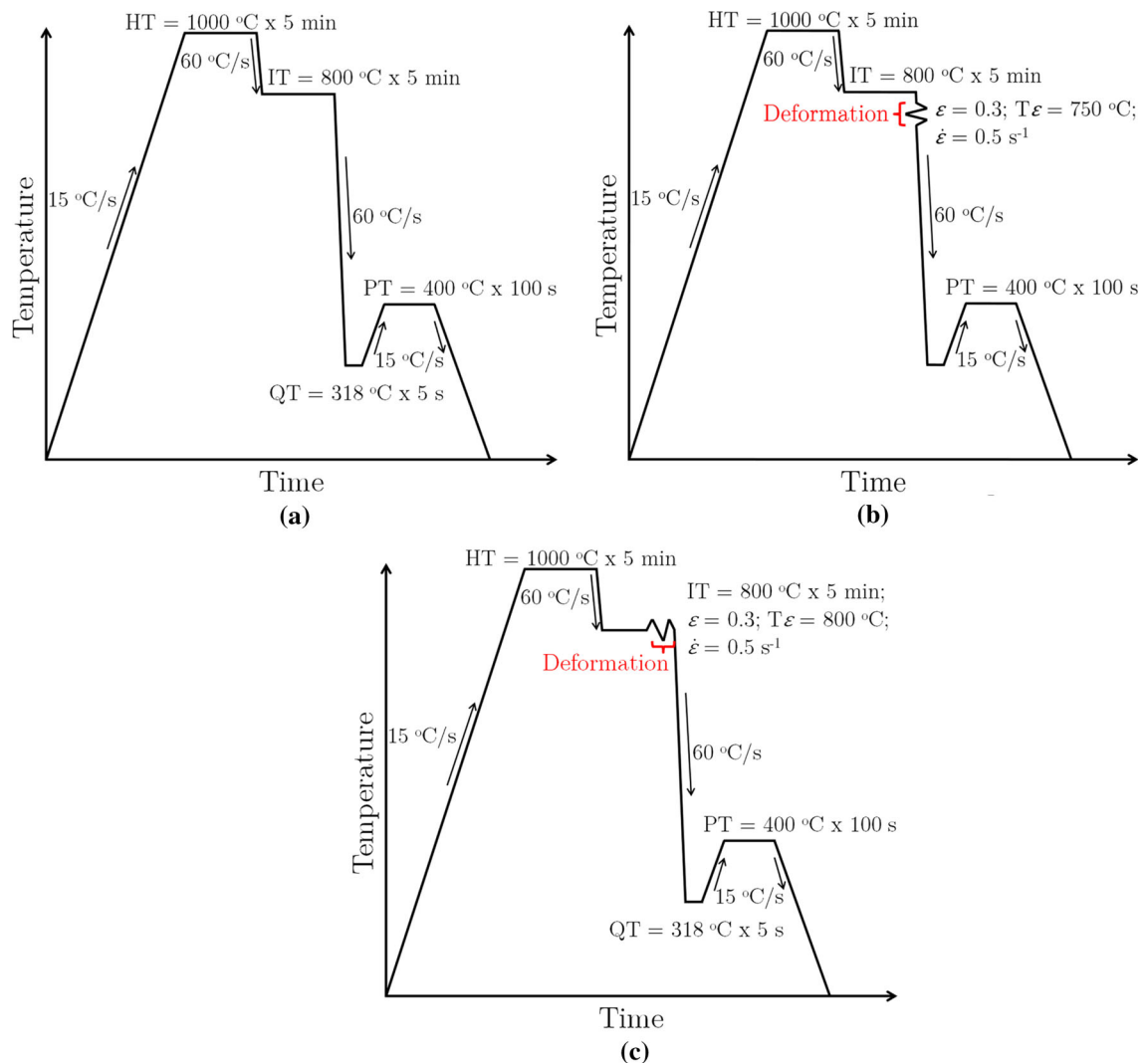
Fig. 1—Schematics of the HSQ&P thermomechanical treatments: (*a*) Q&P; (*b*) HSQ&P, with initial straining temperature at 750 °C; (*c*) HSQ&P, with initial straining temperature at 800 °C. IT, HT, PT, and QT are intercritical, homogenization, partitioning, and quenching temperatures.

down while being simultaneously deformed) and 800 °C (an isothermal process) (Figures 1(b) and (c)). In both cases, the nominal strain rate in both cases was 0.5 s^{-1}, which is commonly used in the hot stamping process.[41] The strain was measured using a non-contact laser dilatometer, which provides real-time measurement of the sample width. The test temperature was monitored using a thermocouple welded on the center of the specimen surface. The optimum quenching temperature (QT), which gives the maximum retained austenite fraction at room temperature at the end of a Q&P process, was estimated according to the constrained carbon equilibrium (CCE) model[18] and based upon the Koistinen and Marburger equation empirically determined in a previous quenching experiment.[34] Therefore, the samples were quenched at 318 °C (QT) for 5 seconds, reheated at 15 °C/seconds to 400 °C, and held for 100 seconds for the partitioning step, and then finally

cooled down to room temperature. The cooling rate during the quenching steps was kept at 60 °C/seconds.

Electron back-scattered diffraction (EBSD) analyses were conducted with an acceleration voltage of 20 keV, a working distance of 15 mm with the specimen tilt angle of 70 deg, and 0.1 μm of scan step size. In order to provide direct evidence that certain regions in the APT and TEM data are indeed austenite, ferrite, and/or martensite, phase identification by combining EBSD and nanoindentation marks was used. Hence, EBSD and nanoindentation tests (which leave distinct markings that are easy to identify but at the same time do not cause high stress concentrations) can be used to find particular microconstituents and interfaces of interest in complex microstructures for further analysis with APT or TEM. Nanoindentations were carried out using the Triboindenter TI 950 in load control testing mode at a constant strain rate of 0.42 s^{-1}.

Table I. Room Mechanical Properties as Determined from Tensile Tests of Q&P and HSQ&P Specimens.[42]

Condition	ε_U (Percent)	ε_T (Percent)	σ_y (MPa)	UTS (MPa)
Q&P	8.9	15	978	1035
HSQ&P$_{750}$	11.5	19	730	835
HSQ&P$_{800}$	13.5	23	820	920

ε_U, ε_T, σ_y, UTS, and δ are uniform elongation, total elongation, yield strength, ultimate tensile strength, and toughness.

The identification of phases was carried out through the correlation of nanoindentation values, image quality (IQ), and kernel average misorientation (KAM). The IQ combined with phase identification was used to distinguish face-centered cubic (FCC) and body-centered cubic (BCC) phases and IQ combined with KAM (calculated for the 5th nearest neighbors of each point and upper limit of 10 deg) was used to distinguish the BCC ferrite and martensite areas.

In this work, the mechanical properties obtained through nanoindentation are not discussed, for details refer to Ariza et al.[34] In Table I, the tensile mechanical properties of the analyzed samples are shown. The methodology used to obtain these results can be found in Ariza et al.[42]

After EBSD/nanoindentation identification, APT was applied for the near-atomic quantitative investigation of carbon partitioning in the Q&P- and HSQ&P-processed TRIP-assisted steel. For APT analysis, site-specific focused ion beam (FIB) lift-outs were taken from regions with a high density of austenite and martensite interfaces. Several sections of the lift-out were mounted on a micro-tip array and each was annularly milled (acceleration voltage of 30 kV) and cleaned (5 kV) with an ion beam to make needle-shaped specimens suitable for field evaporation.[43] APT of the resulting needle-shaped specimens was conducted using a CAMECA Instruments LEAP® 4000X HR local electrode atom probe, which is equipped with an energy-compensating reflectron lens for improved mass resolution. The specimens were field evaporated in laser mode with a 200 kHz pulse repetition rate at the temperature of 30 K, 50 pJ laser power, and a 0.5 to 1.0 pct detection rate. The resulting data were reconstructed and analyzed by means of the CAMECA IVAS software. Gallium damage from the FIB-based specimen preparation method was assessed and removed using the Ga^+ and Ga^{++} isotopes, which was minimized by the 5 kV cleaning step. Deconvolution of the ions within overlapping isobars of different elements (e.g., Cr54/Fe54 and C_2^+/C_4^{++}) was performed based on the natural abundances of the elements.

Specimens were examined by scanning transmission electron microscopy (STEM) using a FEI Talos F200X microscope operated at 200 kV and equipped with an extreme field emission gun (X-FEG) electron source and Super-X EDS (energy dispersive spectroscopy) system with four silicon drift detectors for analysis of the chemical composition. APT and STEM specimens were prepared via the focused ion beam (FIB) milling technique by the in-situ lift-out method using a Hitachi NB5000 FIB-SEM.

III. RESULTS AND DISCUSSION

A. Characterization of the Q&P Sample

Due to the microstructural complexity of the samples after the Q&P and HSQ&P treatments, the results obtained by EBSD and nanoindentation were used to identify the phases, microconstituents, and grain boundaries of interest for further analysis by APT, as shown in Figure 2, for the Q&P sample quenched at 318 °C and partitioned at 400 °C for 100 seconds. In this image, the distribution and size of FCC phase (austenite) are identified by the red-colored areas, whereas the BCC phase (ferrite) is indicated by a green color. This methodology for localization of regions or microconstituents proved to be efficient to be applied in complex microstructures that will later be analyzed by APT or STEM. As expected from the difference in dislocation densities of martensite and ferrite (BCC phase), two distinct image quality regions are observed in the combined IQ and color-coded phase map (Figure 2(a)) and in the KAM map (Figure 2(b)). As state above, the largest lattice defect density in martensite causes a decrease in IQ compared to that of ferrite regions,[44] which enables to identify polygonal ferrite being the light area with high IQ and low KAM and martensite being the dark area with low IQ and a considerable higher degree of local misorientation. In Figure 2(a), it is possible to observe the (two) regions identified for extraction of the lamellae for the APT analysis. In region 1, our interest was to study the concentration of carbon in a ferrite/austenite interface (α/γ, austenite in red), while in region 2, the aim was to quantify the carbon content of a fine retained austenite film (γ_f) between the martensite (α') plates.

Figure 3 shows the APT results of the regions identified with numbers 1 and 2 in Figure 2. Figure 3(a) shows the carbon atom map of a block-form austenite, containing approximately 6.00 at. pct C, extracted from a region between a ferrite grain and a martensite region ($\alpha/\gamma_b/\alpha'$). The carbon content of this retained austenite is considerably higher than the nominal carbon content of the TRIP-assisted steel studied (1.06 at. pct C). This result is close to that recently determined by Poling et al.[45] ($\approx$ 5.7 at. pct), which was also obtained for a block-form retained austenite in a steel subjected to the Q&P process. Poling et al.[45] pointed out that they made several attempts to analyze other regions which included austenite in the form of films, but the attempts were unsuccessful. In Figure 3(b), the APT results of the sample extracted from region 2 are shown. In this figure, it is possible to distinguish martensite with an average carbon content
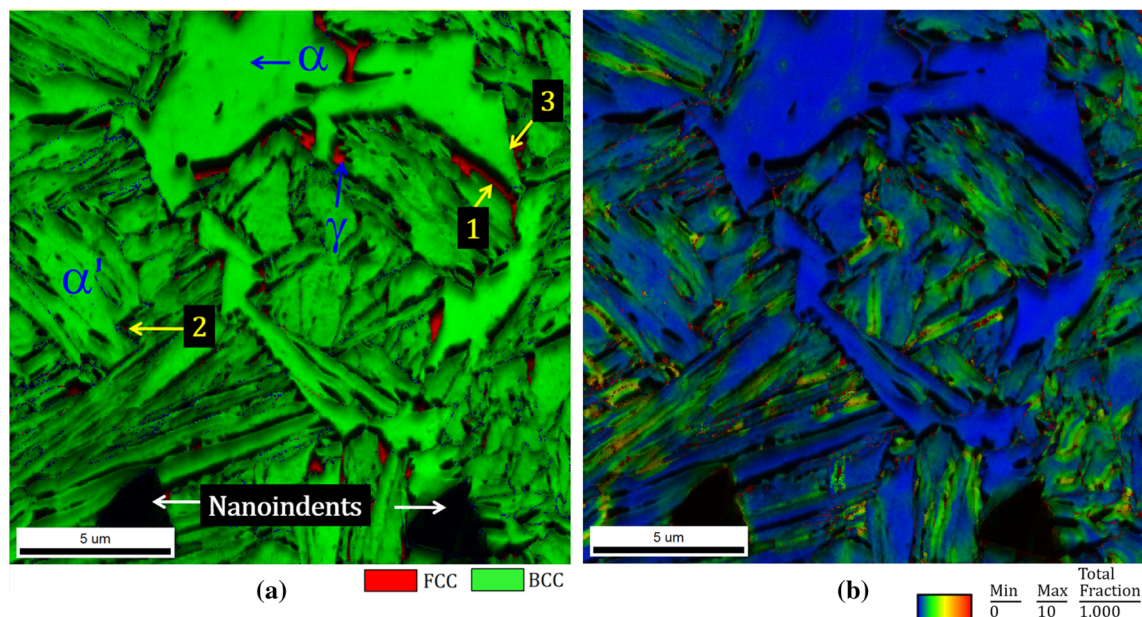
Fig. 2—EBSD phase map and nanoindentations of the Q&P sample, austenitized at 800 °C quenched at 318 °C, and partitioned at 400 °C for 100 s. (*a*) Combined IQ map and color-coded phase map, (*b*) KAM map (Color figure online).

of approximately 0.23 at. pct, a film-type retained austenite (γ_f) with approximately 5.51 at. pct C, and precipitates in martensite with approximately 25 at. pct C, which is most probably cementite (θ, Fe_3C), with the corresponding stoichiometric carbon concentration. These precipitates were most likely formed during tempering of the as-quenched martensite at 400 °C. Toji *et al.*[27] pointed out that precipitation of carbides in martensite can often be seen during the partitioning stage in low and high carbon steels, even when they contain a high amount of Si. On the other hand, HajyAkbary *et al.*,[25] studying the Q&P process in low-carbon steel (0.3 wt pct), found that ε-carbide can be formed in martensite prior to the partitioning stage, during the first quenching.

The atomic fractions of carbon, manganese, and silicon using proximity histograms were estimated by means of isoconcentration surfaces at 2 at. pct. The concentration profiles of the substitutional elements indicate that there was no partition of manganese and silicon between martensite and austenite, so that only the carbon partition occurred during the partition stage at 400 °C for 100 seconds. On the other hand, the silicon behavior in the composition profile of the θ precipitate (bottom part in Figure 3(b)) is compatible with the formation of cementite, since it is well known that due to the low solubility of the silicon in the cementite, its growth must be accompanied by rejection of silicon. The constrained carbon equilibrium (CCE) criterion assumes that all carbon is partitioning from martensite to austenite during the partition stage. Thus, the formation of tempered carbides (such as cementite) is one of the mechanisms that cause a significant deviation of the model, reducing the potential for the carbon enrichment of austenite. The presence of cementite in the martensite, evidenced in the APT measurements, clearly indicates

that the suppression of carbide precipitation considered in the CCE model is not necessarily true, even for steels containing silicon (1.23 wt pct). However, the reaction is markedly retarded to allow significant carbon enrichment in the austenite during the partitioning process and then it enhances the stability of the remaining austenite.

The carbon partitioning evidenced in the proxigrams (histograms of the composition profiles) allows for the identification of phases and grain boundaries. The green boxes in Figure 3 indicate the volumes with which the concentration profiles were measured. In the bottom, proxigram, the concentration profiles of atoms of carbon, manganese, and silicon are presented, starting in martensite (α') and ending in austenite (γ). From this result, it is possible to observe that austenite is significantly enriched in carbon ($C\gamma_f \approx 5.51$ at. pct C), while the martensite is depleted in carbon ($C\alpha' \approx 0.23$ at. pct) in relation to the nominal carbon concentration of the TRIP-assisted steel (1.06 at. pct C). In addition, at the α'/γ interface there is a carbon accumulation of approximately 7.6 at. pct C, implying a negative carbon gradient in the austenite. These results are a strong evidence of the carbon partitioning from martensite to austenite during the partition stage. This phenomenon occurs because the chemical potential of carbon at the interface in supersaturated ferrite (α') is higher than in austenite and both phases have different solubilities. During the partitioning stage, the system aims to balance the chemical potential of carbon, giving rise to a carbon diffusive flux from martensite to austenite. According to the CCE model, the carbon partitioning ends when the metastable equilibrium between ferrite (α') and austenite (γ) is reached, *i.e.*, when the carbon redistribution (partitioning) reaches the point at which the chemical potential of carbon is equal through the α'/γ interface. Thus, the evidence of a carbon concentration
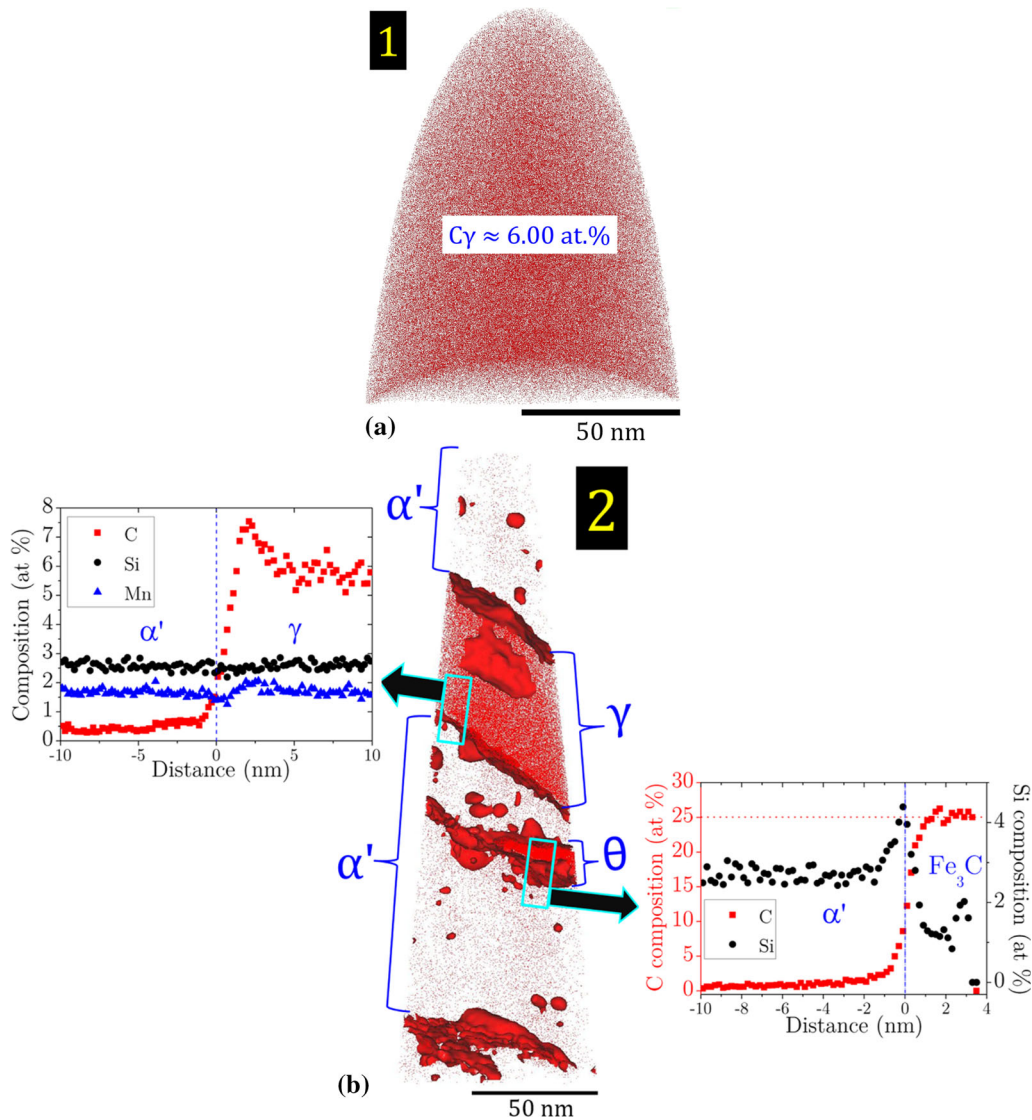
Fig. 3—(a) Carbon atoms map of a block-form austenite, containing approximately 6.00 at. pct C, from the region identified by the number 1 in Fig. 2. (b) Carbon isoconcentration surfaces at 2 at. pct. C superimposed with the carbon atom map (center), for a needle extracted from region 2 in Fig. 2, and proximity histograms obtained across the martensite (α')/austenite (γ) interface (left) and through a cementite (θ or Fe$_3$C)/α' interface (right). The small green boxes show the regions through a carbon cluster and the interface (α'/γ) selected, for carbon, silicon, and manganese concentrations analysis (Color figure online).

gradient at the interface might indicate that the carbon partitioning has not yet reached the steady state.

Estimation of the average time required (t) for the complete homogenization of carbon in the retained austenite from the martensite carbon migration can be obtained by Eq. [1]:

$$t = \frac{\bar{x}}{6D} \qquad [1]$$

with $\bar{x}$ and D denoting the average diffusion distance and the diffusivity of carbon in austenite, which can be expressed as follows:

$$D = D_0 \exp(Q/RT), \qquad [2]$$

where D_0 is the pre-exponential constant (1.00×10^{-5} m^2/s), Q is the activation energy for diffusion of carbon in austenite (135.7 kJ/mol), R is the universal gas constant (8.314 J/K·mol), and T is the absolute temperature (K). For the calculations of the homogenization time, it is assumed that the average diffusion distance is equivalent to the austenite film thickness, i.e., ≈ 50 nm, according to Figure 3. Application of Eq. [1] leads to a homogenization time, at the quench temperature (318 °C), of 41.4 seconds, while the holding time at that temperature was only 5 s. De Knijf et al.[46] suggested that, at the quenching temperature, the isothermal holding time at the quenching temperature in Q&P steels must be kept short (usually five to ten seconds) to prevent the precipitation of isothermal transformation products. The same type of calculation applied at the partitioning temperature (400 °C) leads to a partition time of ≈ 1.43 seconds for complete homogenization of carbon in austenite. However, as shown in

Figures 2 and 3(a), there are regions of austenite (blocky) up to 0.5 μm thick, for which a homogenization time of 142.9 seconds during the partitioning stage is required. It is worth mentioning that this simplified calculation does not consider either the effect of carbides precipitation in martensite or the composition dependence of carbon diffusivity in austenite. It is known that carbon diffusivity in austenite is exponentially increased with increasing carbon contents.[47] By applying a recent numerical model[48] for the kinetics of carbon partitioning, which considers such effect, the prediction for the homogenization time is approximately five times faster than the analytical results. Furthermore, it is expected that carbides precipitation retards the carbon partitioning because they must be first dissolved in order to carbon be segregated to austenite.[25] Additionally, the presence of carbides in martensite decreases the difference of chemical potentials of carbon between the austenite and the mixture martensite + carbides. At the moment, there is no quantitative model available including all these effects.

With regard to the effect of the austenite morphology on the carbon content, the retained austenite in blocky type (γ_b) presents a higher concentration of carbon in relation to austenite in the film-type (γ_f): $C\gamma_b \approx 6.00 \pm 0.01$ at.pct and $C\gamma_f \approx 5.51 \pm 0.02$ at. pct. This can be explained by the contribution of carbon enrichment (in blocky austenite) of both ferrite and martensite. In addition, the cementite formation observed in martensite in the vicinity of film-like austenite has a direct influence on the available carbon to be partitioned from martensite.

B. Characterization of the HSQ&P Sample Strained at 750 °C

The APT results, for the sample HSQ&P strained at 750 °C in 30 pct (true strain) at a rate ($\dot{\varepsilon}$) of 0.5 s^{-1}, quenched at 318 °C, and partitioned at 400 °C for 100 seconds, are presented in Figure 4. In this figure, distribution and size of the retained austenite are indicated by the red regions, while the ferrite and martensite appear green. In Figures 4(a) and (c), it is observed that the grains with higher subgrain boundaries always have relatively lower IQ values. Hence, owing to a less perfect BCC phase, martensite can qualitatively be distinguished from ferrite by darker regions with a lower image quality based on the very high dislocation density in martensite.[44,49,50] This enables identifying martensite (α'), ferrite (α), and austenite (γ) in Figure 4. The yellow rectangles indicate the regions from which the needles were extracted by FIB for further analysis by the APT.

Comparing the EBSD phase maps in Figure 4 with that of the sample submitted to the Q&P treatment (Figure 2), it can be seen how the high-temperature deformation promotes the reduction of the grain size of both ferrite and martensite, which could contribute to improving the relation of tensile strength and ductility of the TRIP-assisted steel analyzed.

The identification of the nanoindentation values in the EBSD images makes it possible to relate the values of nanohardness with the analyzed regions and, in this way, to identify the grains of ferrite, martensite, and austenite present in the analyzed volume. The map of the carbon atoms of an α/γ interface and its local composition profile by proximity histogram of carbon, silicon, and manganese are shown in Figure 4(b). The results of the composition profile showed a significant carbon enrichment in austenite ($C\gamma \approx 6.63 \pm 0.01$ at. pct), while the results for silicon and manganese did not show an evident partitioning at the α/γ interface. In Figure 4(b), a carbon accumulation at the α/γ interface (≈ 9.45 at. pct) was also observed. In order to analyze if there was a carbide precipitation into the martensite under the heat treatment conditions studied here, an APT measurement was conducted on a needle extracted from the region clearly delimited as martensite by the blue contour dotted in Figure 4(c), specifically at the region delimited by the yellow rectangle. Figure 4(d) shows the composition profile of Si, C, and Mn at the interface of the cluster indicated by the blue arrow at the carbon isoconcentration surface at 7 at. pct C superimposed with the carbon atom map. This result reveals that the Si concentration is homogeneous in both α' and the cluster, indicating that it is probably a preferential agglomeration of carbon atoms instead of a cementite particle. In addition, the cluster has a lower carbon content (≈ 15 at. pct) than expected for a stable precipitate such as cementite (≈ 25 at. pct), or for transition carbides (metastable) such as ε-carbide (≈ 33 at. pct), Fe2,4C (hexagonal), or the η-carbide (≈ 29 at. pct). Timokhina et al.[51,52] identified low-temperature carbides having carbon contents between 10 and 20 at. pct in a dual-phase steel, such as $Fe_{32}C_4$ or $Fe_4C_{0.63}$. These carbides were associated with the bainitic-ferrite formation during the isothermal transformation at low temperatures (≈ 200 °C), for long holding times (10 days), during the bake-hardening process and pre-strained to 5 pct. However, in the present study, the region where these clusters were identified was clearly identified by EBSD and nanoindentation as martensite. In addition, the low-carbon martensites consist of laths, separated by low- or high-angle boundaries, but containing a high dislocation density between them.[53] It is known that grain boundaries and dislocations can act as sinks for carbon atoms due to the reduction of the chemical potential of carbon at these defects,[54] which results in local carbon enrichment in these regions. Therefore, the clusters observed in Figure 4(d) are likely to correspond with the carbon segregation at the boundaries of the martensite laths. It is important to take into account that atom probe tomography measurements are very localized accounting for volumes with lengths in the 10 to 100 seconds of nms with a maximum radius of ≈ 50 nm. At other locations, carbide formation could happen in HSQ&P$_{750}$ sample, however, it was not possible to observe carbide formation by APT or STEM techniques in this sample.

It is important to note (in Figure 4(d)) that the carbon clusters seem to align themselves in one single habit plane, or preferential invariant planes at the interface
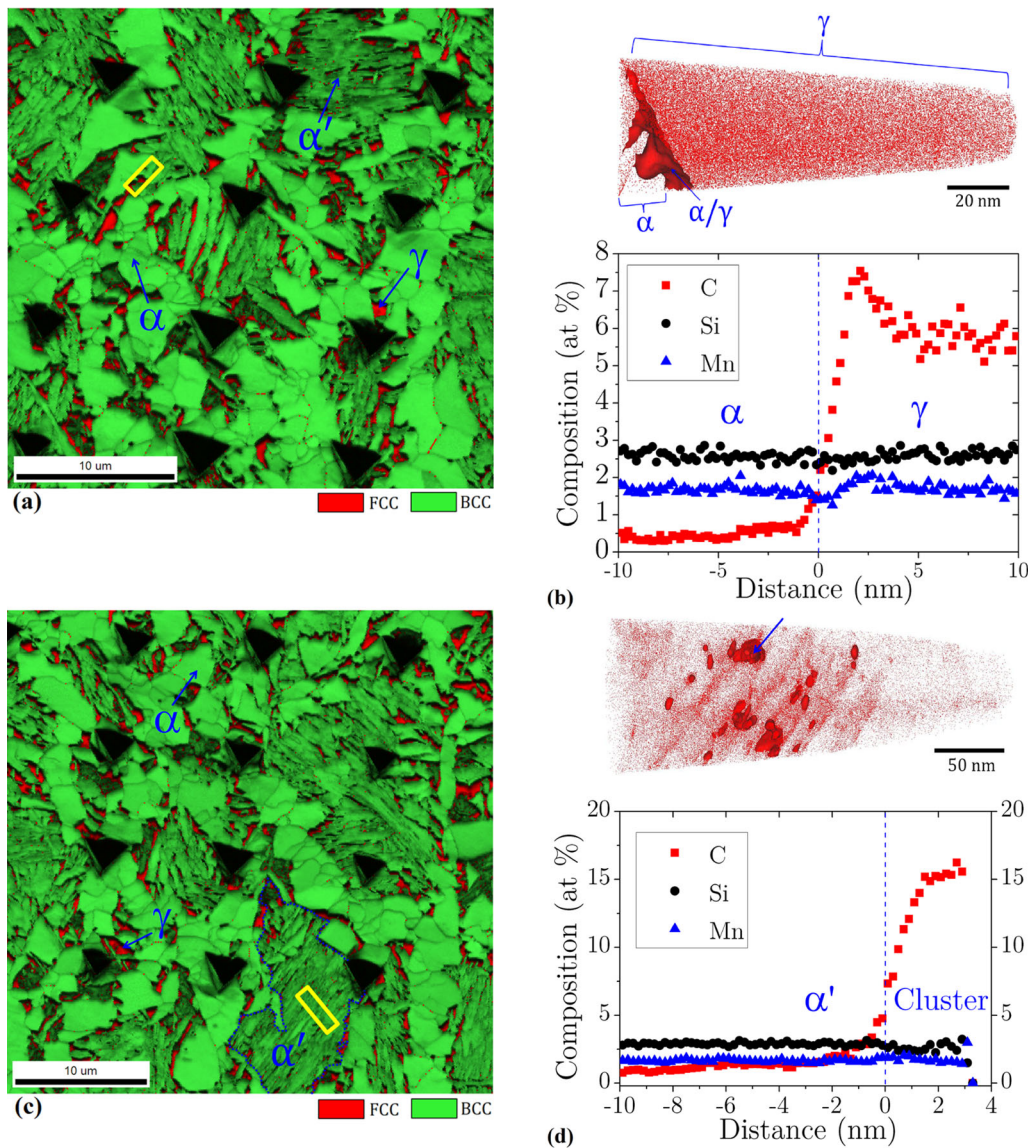
Fig. 4—Results for HSQ&P sample strained at 750 °C in 30 pct at a rate of 0.5 s^{-1}, quenched at 318 °C, and partitioned at 400 °C for 100 s. (*a*) EBSD phase map of the HSQ&P$_{750}$ sample with nanoindentations, (*b*) 3 at. pct C isoconcentration surface for a ferrite (α) and austenite (γ) interface extracted from the region indicated in yellow rectangle in (a), and proxigrams obtained through the α/γ interface; (*c*) EBSD phase map of the HSQ&P$_{750}$ sample with nanoindentations. Martensite region is delimited by blue contour; (*d*) carbon isoconcentration surface at 7 at. pct, in the martensite region identified in the yellow rectangle in (c) and proxigrams obtained through the α'/C-cluster interface identified by the blue arrow. APT needle-shaped samples were cut from the regions highlighted by yellow rectangles (Color figure online).

along which the martensite laths form. The characteristics of the parallel plates could correspond with the carbon segregation to stacking faults or microtwins in martensite, as observed by transmission microscopy (yellow arrows in Figure 6). Another explanation is that this alignment could be caused by the applied stresses, which favor the formation of preferential crystallographic variants on the planes of the maximum shear stress planes.[55] Therefore, due to the fact that there are many crystallographic variants available per austenite grain, there is a high probability that the orientation of a plate is close to the preferred orientation for the alignment to occur with respect to the stresses.[56] It is worth noting that the presence of such agglomeration of carbon or the formation of precipitates in martensite

reduces the levels of carbon available to enrich the austenite and stabilize it at room temperature.

Comparing the blocky-type austenite carbon contents (at an α/γ_b interface) of the HSQ&P sample strained at 750 °C ($C\gamma_b \approx 6.63 \pm 0.01$ at. pct) and the Q&P sample ($C\gamma_b \approx 6.00 \pm 0.01$ at. pct), both quenched at 318 °C and partitioned at 400 °C for 100 seconds, it is possible to observe an increase of ≈ 10 pct in the carbon content for the HSQ&P sample. This result can be explained by the additional contribution (besides the portion of carbon depletion of the supersaturated martensite in the partitioning step) in the austenite carbon enrichment caused by the migration of carbon from the ferrite created during the deformation at high temperature, *i.e.*, formed by the DIFT effect.[39,57] This is a combined increase

effect of both the driving force produced by the deformation stored energy in the deformed austenite to produce the ferritic transformation, and the number of nucleation sites caused by the increase in the dislocation density induced by the deformation. Therefore, the amount, rate, and temperature of deformation can have a significant effect on this type of transformation. It can be seen that the deformation of the austenite at high temperatures promotes a diffusional phase transformation (also proven by the higher amount of ferrite in the HSQ&P, $\approx$ 41 pct, sample when compared to the Q&P, $\approx$ 21 pct), which causes a higher carbon enrichment in the untransformed austenite and the decrease of the M_s temperature ($M_{s\text{-Q\&P}} = 390$ °C, $M_{s\text{-HSQ\&P}(\varepsilon\ =\ 750\ °C)} = 372$ °C).

In Figure 5(a), the dark green regions identify areas of lower image quality (IQ), which are probably due to a high dislocation density, and might be fresh martensite, α'_f (martensite created during the second quenching step).[58] These regions are correlated to grains containing a greater concentration of lattice imperfections, for example, point defects and dislocations, which result in low blurred Kikuchi band edges contrast and contrast, and hence lower quality index diffraction patterns.[34] Moreover, tempered martensite in form of laths may be larger size than α'_f, since it can transform across the whole austenite grain, while α'_f has to transform within smaller austenite grains after the partitioning stage. In Figure 5(b), it can be observed that the high local misorientation in the fresh martensite blocks is identified by the darker green color in the image quality map, while the areas in blue (*i.e.*, average misorientations varying between 0 and 2 deg) correspond to ferrite

regions with higher IQ values. These analyzed regions were selected from the phase map obtained by EBSD (Figure 5). The STEM results of the regions identified with numbers 1 and 2 in Figure 5 are shown in Figures 6 and 7, respectively.

Figure 6(a) corresponds to the surface indicated by the yellow rectangle, labeled #1, in Figure 5 where an α'_f/α interface is identified. The appearance of carbon enrichment in austenite (Figure 6(b)) demonstrates that carbon partitioned from martensite to retained austenite during partitioning stage at 400 °C. However, if the degree of carbon enrichment in retained austenite is not sufficiently high to reduce the martensite start temperature below room temperature, part of the retained austenite transforms into twinned martensite during final cooling from 400 °C to room temperature (Figures 6(c) and (d)). In the central part of Figure 6, a martensite grain embedded between ferrite grains was identified. For comparison, Figures 6(e) and (f) show STEM Dark-Field and High-Angle Annular Dark-Field STEM (HAADF-STEM) images, respectively, obtained in HSQ&P750 sample. The HAADF-STEM image in Figure 6(f) is taken from the same area as the bright-field image in Figure 6(a), neither image reveals carbide precipitation in this sample. The magnification of one of the central regions of the microstructure also presents characteristics typical of twinned martensite (Figure 6(e)), related to the transformation that occurs in steels with high carbon concentration. This shows that, after the partitioning step, part of the austenite, having enough carbon to stabilize it at room temperature, remains as retained austenite, while the lower carbon content part, not completely stabilized, may transform to untempered twinned martensite.
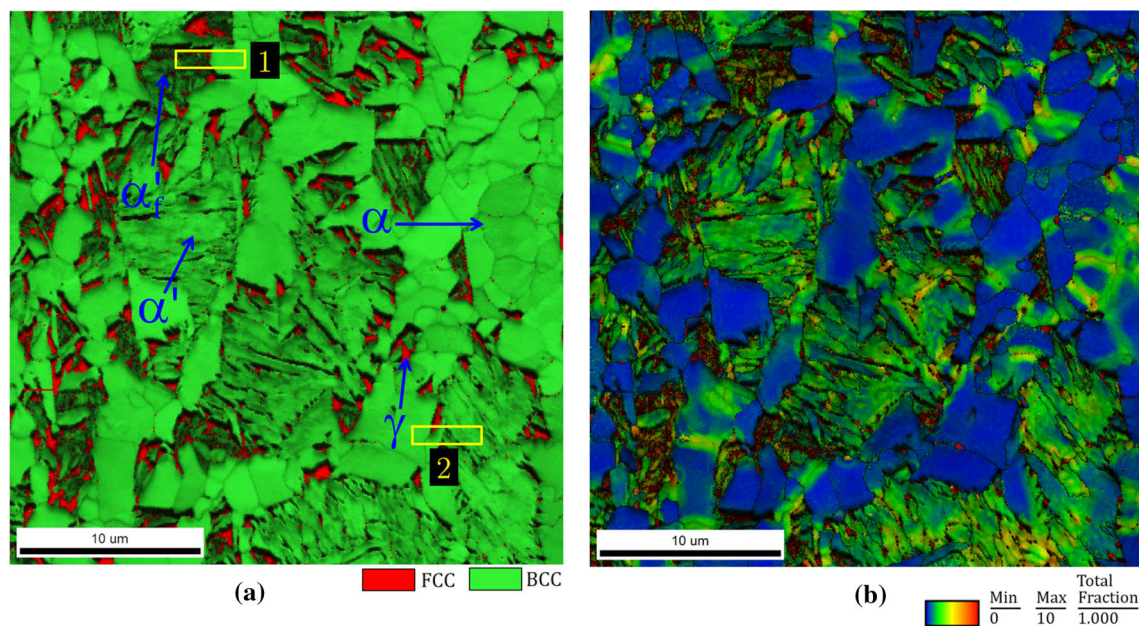

Fig. 5—(*a*) Combined IQ map and color-coded phase map identifying the regions corresponding to ferrite (α), martensite (α'), and retained austenite (γ). The distribution of γ is identified by the red regions, whereas the α and α' phases appear as green. (*b*) Combined IQ and KAM map. HSQ&P sample strained at 750 °C in 30 pct at a rate of 0.5 s^{-1}, quenched at 318 °C, and partitioned at 400 °C for 100 s (Color figure online).
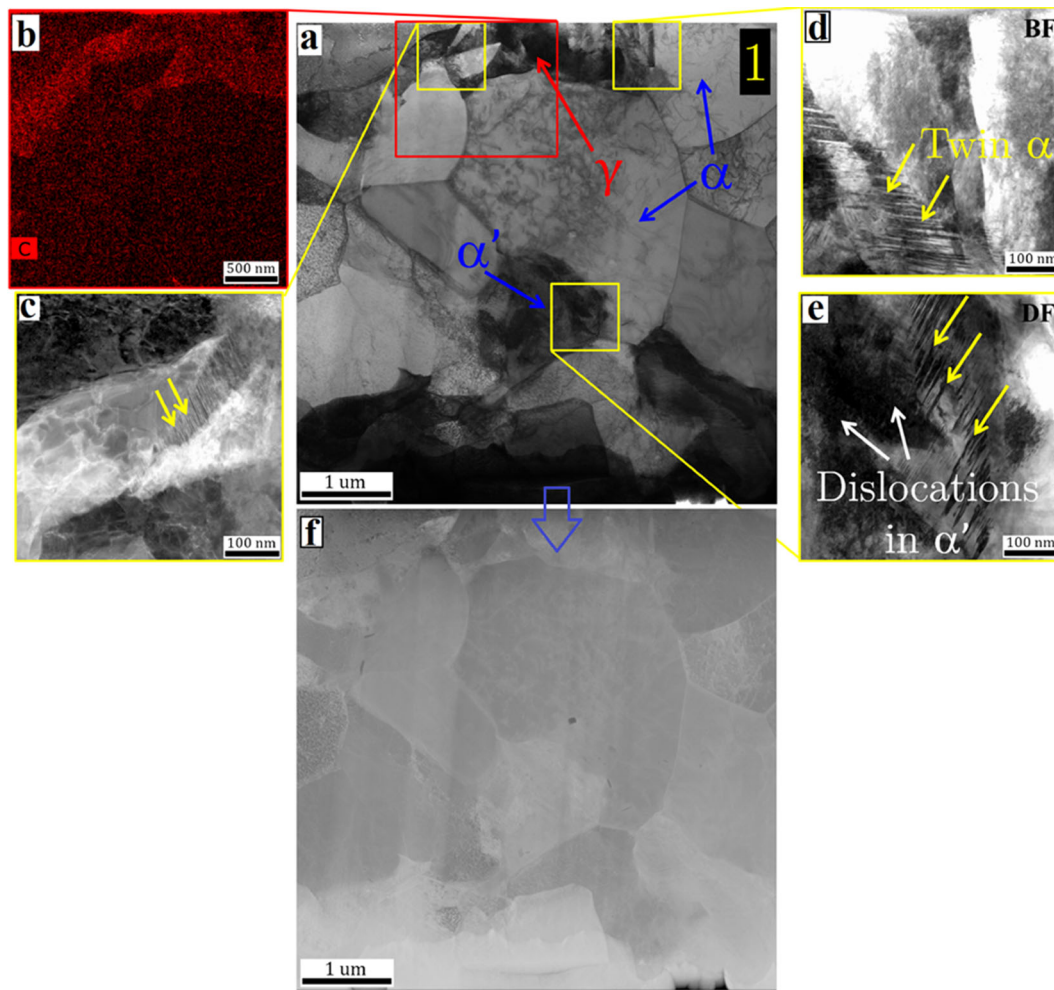
Fig. 6—(*a*) BF-STEM image of the region 1 identified in Fig. 5 of the HSQ&P sample strained at 750 °C in 30 pct at a rate of 0.5 s^{-1}, quenched at 318 °C, and partitioned at 400 °C for 100 s. (*b*) The carbon map (in red) obtained by energy X-ray dispersive spectroscopy (EDS). In the images with a yellow border (*c* through *e*), twinning regions are identified by the yellow arrows. (*e*) STEM Dark-Field (DF) image shown in the inset of Figure (a); and (*f*) High-Angle Annular Dark-Field STEM (HAADF-STEM) image identifying region 1. γ, α′, and α are austenite, martensite, and ferrite, respectively (Color figure online).

The images obtained by STEM of the sample extracted from region #2 are analyzed in Figure 7. Figure 7(a) shows a bright-field (BF) STEM image of the typical interlath retained austenite (γ) with a film-like morphology (dark films) located between the martensite lath boundaries. The identification of retained austenite, ferrite, and the two types of martensite, lath martensite and twin martensite (Figures 6 and 7), is similar with previous work[59–64] also performed in steels treated by Q&P heat treatments. The presence of adjacent martensite (which formation induces defects in the surrounding austenite) and the early stage of tensile deformation during the HSQ&P process may explain this result. EDS elemental maps of carbon and manganese are shown in Figures 7(c) and (d). It is possible to observe that the austenite films between the laths of martensite are enriched in carbon, evidencing the partition of carbon. Furthermore, it is observed that carbon-enriched austenite has a saw-tooth morphology, so that in the vicinity of the interface with ferrite the carbon enrichment is higher. This result shows that the presence of

ferrite has an important role in the carbon enrichment of austenite. A possible explanation for this phenomenon is the pre-existence of a carbon accumulation in the vicinity of the original ferrite/austenite interface. The existence of this accumulation is possible if the formation of the ferrite has not reached equilibrium or if there was not enough time for the carbon to homogenize in the austenite. As the DIFT ferrite formation occurs rapidly during the straining process (duration of 0.6 seconds), both considerations are compatible with the experimental results. In relation to the distribution of manganese in the analyzed region (region #2), a significant accumulation of Mn along the ferrite/marten-site interface (original austenite) was observed. How-ever, it is not possible to observe a significant difference in the content of Mn in the volume (far from the interface) between martensite (austenite) and ferrite, although the partitioning of Mn can be thermodynam-ically predicted. This partition limited to the interface can be associated with two phenomena: the occurrence of a solute drag effect at the interface during ferrite
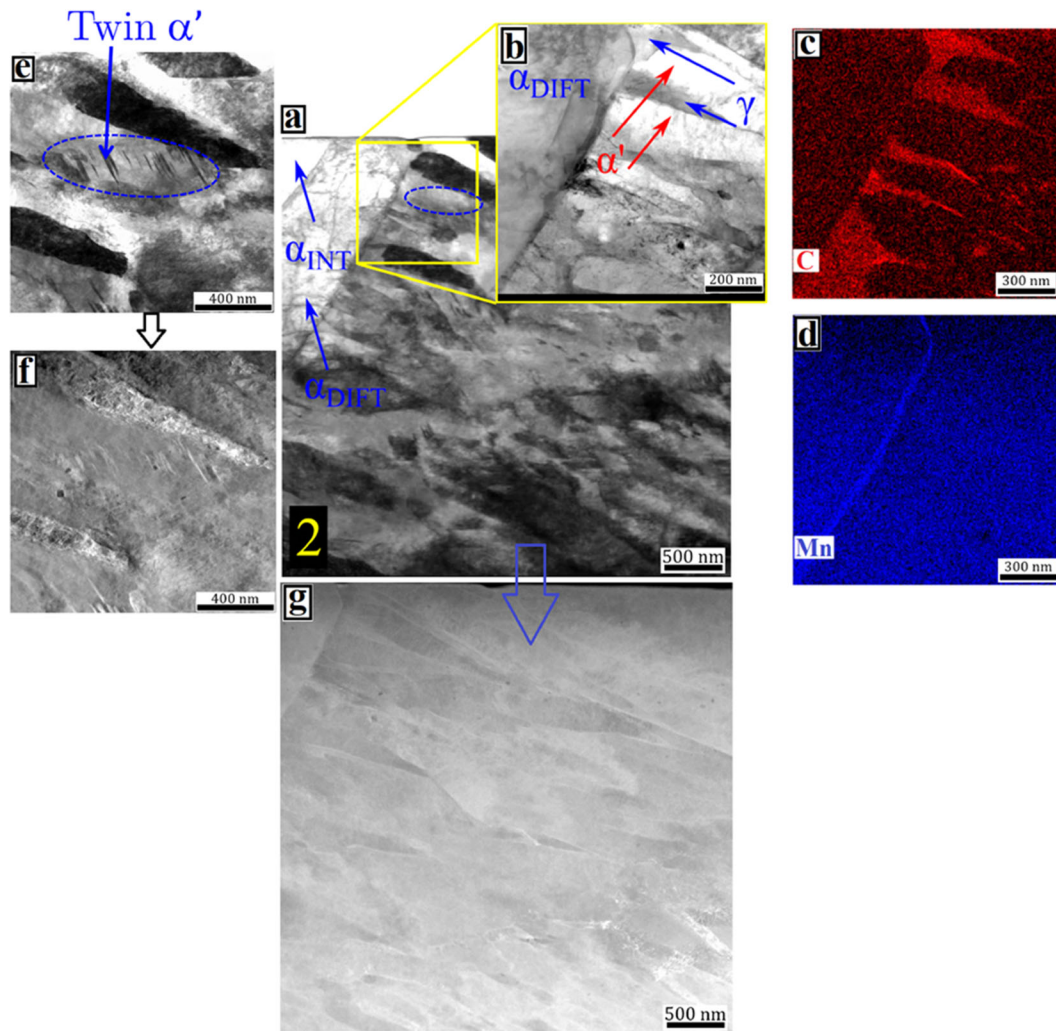
Fig. 7—(a) BF-STEM Image obtained by STEM of region 2 identified in Fig. 5 of the HSQ&P sample strained at 750 °C in 30 pct at a rate of 0.5 s^{-1}, quenched at 318 °C, and partitioned at 400 °C for 100 seconds. In the inset with the yellow border expanded (b), the bright-field STEM image showing the DIFT ferrite, the lath martensite, and interlath austenite. (c and d) Corresponding EDS elemental maps of carbon (C, in red) and manganese (Mn, in blue). (e) Zoom in BF-STEM image of the region marked in blue oval in Fig. 6(a) showing twin α'. (f) and (g) High-angle annular dark-field STEM (HAADF-STEM) images. α', α$_{\mathrm{INT}}$, α$_{\mathrm{DIFT}}$, and γ are martensite, intercritical ferrite, DIFT ferrite, and austenite, respectively (Color figure online).

growth, or the kinetic control regime known as local equilibrium with negligible partitioning (LENP). The LENP regimen will be discussed in the next section. Additionally, Figures 7(f) and (g) show the HAADF-STEM images. The HAADF-STEM image in Figure 7(f) is taken from the same area as the bright-field image in Figure 7(e) and Figure (g) is taken from the same area as the bright-field image in Figure 7(a) obtained in HSQ&P$_{750}$ sample of region 2 identified in Figure 5. The dense, dark regions seen in Figure 7(e) are equal to the illuminated regions as seen in the Dark-Field image (Figure 7(f)); these regions are retained austenite, and correspond with the carbon-enriched regions observed in Figure 7(c).

The BF-STEM image of HSQ&P sample (Figure 7) confirms the concurrence presence and stabilization of the thin films of retained austenite distributed along the carbon-depleted martensite (formed during Q&P stage). The thin-film morphology of retained austenite is considered to favorably influence on the toughness and ductility.[65] Additionally, it is known that one of the important strengthening mechanisms in Q&P steels is the martensite dislocation strengthening.[66]

C. Characterization of the HSQ&P Sample Strained at 800 °C

The APT results of the HSQ&P sample strained at 800 °C in 30 pct at a rate of 0.5 s^{-1}, quenched at 318 °C, and partitioned at 400 °C for 100 seconds are shown in Figure 8. Figure 8(a) shows the EBSD phase image identifying the indentations that allowed the three regions of interest (α, ferrite, α', martensite and γ, retained austenite) to be located for APT analysis. As shown in Figures 8(a) and (b), the austenite evaluated in region #1 at an α'/γ interface in the vicinity of a ferrite grain is significantly enriched in carbon (C$\gamma \approx$ 7.3 at. pct), indicating that there was carbon partitioning from

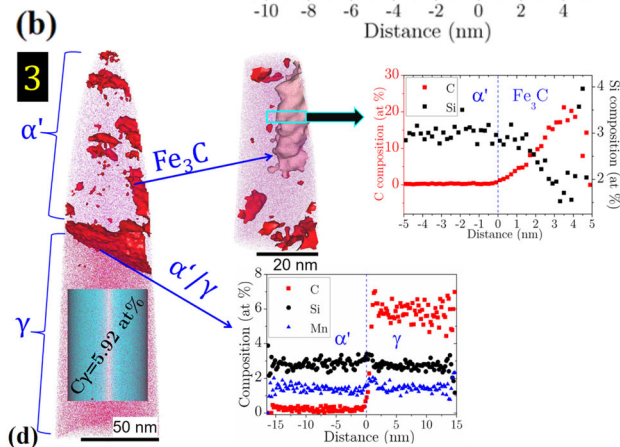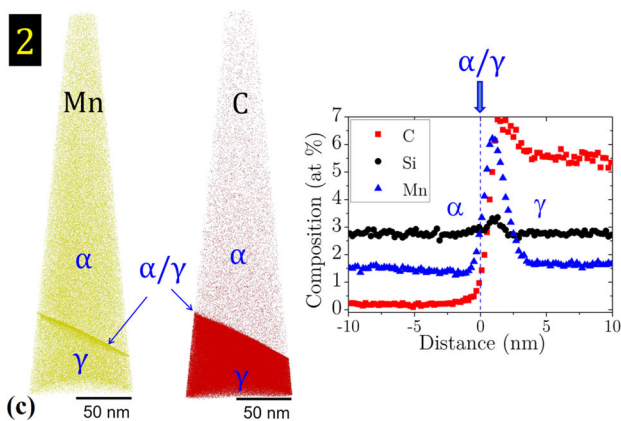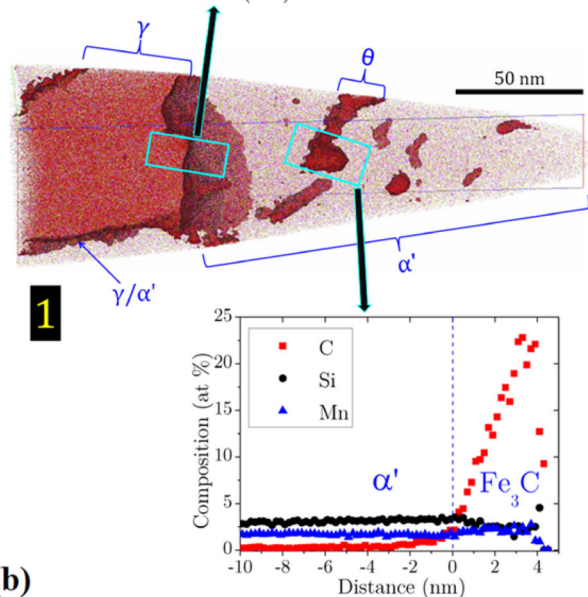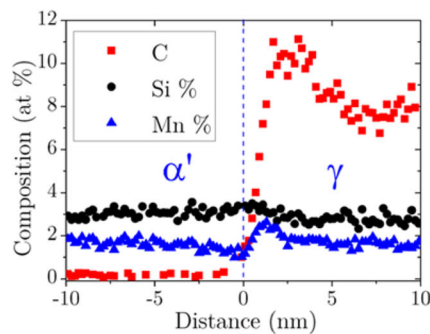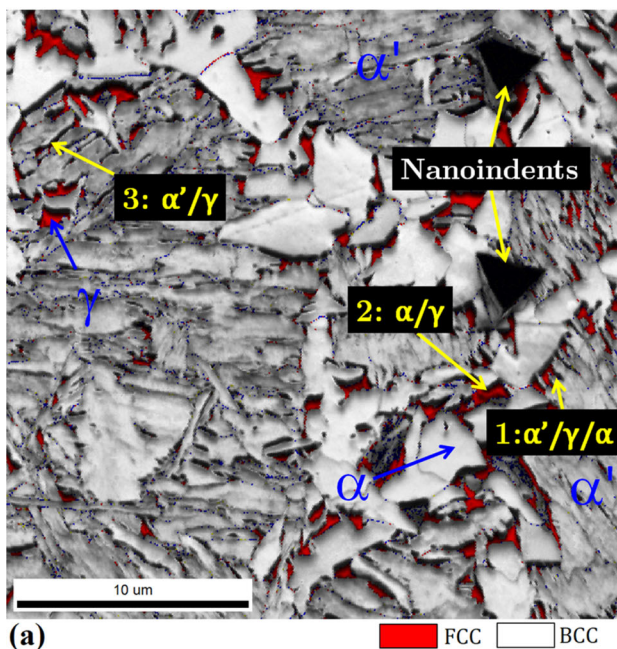Fig. 8—HSQ&P sample strained at 800 °C in 30 pct at a rate of 0.5 s^{-1}, quenched at 318 °C, and partitioned at 400 °C for 100 s. (*a*) EBSD image identifying the nanoindentations that allowed the regions of ferrite (α), martensite (α'), and retained austenite (γ) to be located; (*b*) carbon isoconcentration surfaces at 3 at. pct C, superimposed with the carbon atom map (center), for a needle extracted from region #1, and proximity histograms obtained across α'/γ interface (top) and through a Fe$_3$C/α' interface (bottom). (*c*) Mn and C atom maps and proximity histogram across α/γ interface of the region identified as number #2 in image (a). (*d*) Carbon isoconcentration surface at 3 at. pct C for an α'/γ interface, identified with the number #3 in image (a), superimposed with the carbon atom map, and proxigrams through a $\alpha'/$Fe$_3$C and α'/γ interfaces.

martensite to austenite. As previously pointed out, the carbon accumulation during the formation of DIFT ferrite may also contribute to the carbon enrichment of austenite.

At the α'/γ interface obtained in region #3 (Figure 8(d)), far from the influence of the ferrite grain, carbon accumulation at the interface ($C\alpha'/\gamma \approx 7.3$ at. pct) was also observed; however, it is less than that

observed at the interface obtained in region #1 ($C\alpha'/\gamma \approx$ 11 at. pct), as can be seen in Figure 8(b). In addition to the characterization of region #1, this result strongly indicates that the presence of ferrite in the surroundings affects the carbon content of the retained austenite ($C\gamma$), since $C\gamma$ at the $\alpha'/\gamma/\alpha$ interface was 7.3 at. pct, while at the α'/γ interface this value was 5.9 at. pct. In this figure (Figure 8(b)), the proxigram obtained through an

θ/α' interface is also presented. The carbon content determined at θ was ≈ 23 at. pct, below the nominal composition of the cementite (25 at. pct), and may be a result of artificial Carbon loss within the atom probe experiment. However, the silicon rejection observed in this carbon agglomeration region (bottom part of Figure 8(b)) suggests that the identified phase is cementite (Fe_3C). Due to the high driving force for precipitation of carbides from the carbon supersaturated martensite, carbide precipitation is practically unavoidable. Thus, the partitioning of carbon from martensite to austenite and the tempering phenomenon occur simultaneously, but they are not mutually exclusive under the thermomechanical treatments carried out. Consequently, one of the main considerations of the CCE model—the absence of cementite formation during the partitioning stage—is violated.

The amount of carbon loss, mentioned previously, changes for different experimental parameters and carbon-containing phases. Carbon is lost because it is not detected, and therefore, it is difficult to quantify the error. At the moment, an accurate or standard method for quantifying C loss has not been determined. However, the experimental procedures were consistent between samples so that the C content for the same phase could be compared between samples.

The results of the α/γ interface analysis obtained in region #2 are shown in Figure 8(c). The measured carbon contents in γ and α in this region were $\approx 5.22 \pm 0.01$ at. pct and $\approx 0.02 \pm 0.00$ at. pct, respectively, while an accumulation of $\approx 6.09 \pm 0.1$ at. pct at the interface was observed. However, although the same concentration of Mn in α and γ in the analyzed volume was observed, a high Mn enrichment at the interface was observed. As previously reported, such behavior may be associated with either a solute drag effect or ferrite growth under local equilibrium with negligible partitioning (LENP).[67] LENP assumes that a full local equilibrium is achieved, and a very thin Mn spike is supposed to build at the α/γ interface. In order to evaluate if the width of the Mn peak is compatible with the LENP regime, Eq. [3] can be used to estimate the time required for such a peak to develop. Sun and Pugh[68] suggest that the diffusivity of manganese in austenite (D_{Mn}^γ) can be calculated by the expression (measured in cm^2/s):

$$D_{Mn}^\gamma = 0.16 \exp\left(-\frac{261700}{RT}\right). \qquad [3]$$

Applying the diffusivity calculated at 800 °C and the Mn peak width estimated as 3 nm, from Eq. [3], 0.51 s it is obtained, a value close to the time interval of the deformation step in which the DIFT ferrite is formed.

It is necessary to note that the austenite analyzed in the region 2 of the HSQ&P$_{800}$ sample was taken from a region surrounded completely by ferrite, in such a way that martensite has no influence on the carbon enrichment of this austenite. As seen in the other samples (region 1 of the Q&P showed in Figure 3(a) and HSQ&P$_{750}$ in

Figure 5(a)), the γ/α interface has been additionally influenced by martensite, increasing the carbon content.

The carbon enrichment of the austenite at the α/γ interface (proximity histograms in Figures 8(b) and (c)) is produced mainly by the migration of carbon atoms coming from the ferrite growth, and in the regions far away from the interface, where there is no diffusionally enriched zone by the phase growth, the carbon content in the austenite is a consequence of the intercritical annealing condition imposed on the heat treatments. The carbon enrichment at the interfaces in both treatments (Q&P and HSQ&P) can also be explained by Fick's Law, where the diffusion flux is oriented towards a gradient of chemical composition. Therefore, if there was not this composition gradient and difference in phase solubility (in martensite the solubility of carbon is much lower and the diffusion rate is higher), the observed partitioning of carbon would not be possible. Another explanation could be the fact that grain boundaries and dislocations (the carbon atoms are trapped at dislocations present in the interface) act as sinks for carbon due to the reduction in the chemical potential of carbon at the defects (carbon segregation at the stacking faults).

In the sample submitted to the HSQ&P process with straining at 800 °C, an increase in ferrite content of ≈ 10 pct was observed. This increase in DIFT ferrite (α_{DIFT}) or the strain-induced transformation (SIT) phenomenon, which is attributed to the acceleration of the nucleation rates and ferrite growth after the intercritical deformation, leads to a higher carbon content available to diffuse (since the solubility of carbon in the austenite is higher than that in the ferrite) in austenite. This behavior of the carbon redistribution also allows us to understand the presence of the twinned substructure (mainly at the interfaces) observed by transmission electron microscopy in the deformed sample, as indicated by the yellow arrows in Figure 6. Additionally, a consequence of the higher carbon enrichment in the HSQ&P samples is that this retained austenite becomes chemically more stable as a result of the reduction in the M_s temperature, which increases the capacity of the material to undergo the transformation-induced plasticity (TRIP) effect. Hence, in HSQ&P samples, the carbon partitioning into austenite from supersaturated martensite, intercritical ferrite, and ferrite induced by deformation are essential for austenite stabilization. The knowledge of these effects is essential for the understanding of the phase composition and morphology of the final microstructure and, therefore, the final properties of the material.

IV. CONCLUSIONS

1. Due to the microstructural complexity of the samples after the Q&P and HSQ&P processes, the combined use of EBSD and nanoindentation for the identification and characterization of regions of interest for further analysis by APT and STEM proved to be very useful.

2. It was possible to confirm the significant carbon enrichment of the austenite after the Q&P and HSQ&P processes, and depletion in carbon content in the martensite, which confirmed the carbon partitioning phenomenon during the partitioning step.
3. The results of the Q&P sample for a film-like retained austenite indicated a percentage of carbon of 5.51 ± 0.02 at. pct and 0.23 ± 0.00 at. pct in martensite, with a considerable carbon accumulation at the α'/γ interface (7.6 ± 0.1 at. pct). In the martensite region, precipitation of cementite was also observed.
4. Blocky austenite of the Q&P sample had a carbon content of $\approx 6.00 \pm 0.01$ at. pct. The comparison between the carbon contents of film-like interlath retained austenite (between martensite plates) and blocky retained austenite allowed us to confirm that the increase of the carbon content in the blocky type is a result of the contribution in the carbon enrichment of both martensite and ferrite during the partition stage.
5. In both Q&P and HSQ&P samples, significant carbon build-up at the interfaces was observed. Thus, the grain boundaries and dislocations may act as sinks for carbon due to the reduction in the chemical potential of carbon at defects.
6. The HSQ&P samples showed the highest carbon enrichment in the austenitic phase when compared with the Q&P sample. The main reason for this higher carbon enrichment in HSQ&P samples is the contribution of the formation of proeutectoid ferrite, the formation of DIFT ferrite, and the carbon partitioning into austenite from the supersaturated martensite, while the Q&P sample only receives a carbon contribution from the formation of proeutectoid ferrite and the martensite during the partition stage.
7. A manganese concentration spike at an α'/γ interface was observed by APT and STEM. This is a strong evidence that the growth of proeutectoid ferrite occurs under local equilibrium conditions with negligible partitioning (LENP).

REFERENCES

1. C. Wang, H. Ding, M. Cai, and B. Rolfe: *Mater. Sci. Eng. A*, 2014, vol. 610, pp. 436–44.
2. R. Blondé, E. Jimenez-Melero, L. Zhao, N. Schell, E. Brück, S. van der Zwaag, and N.H. van Dijk: *Mater. Sci. Eng. A*, 2014, vol. 594, pp. 125–34.
3. J.-C. Hell, M. Dehmas, S. Allain, J.M. Prado, A. Hazotte, and J.-P. Chateau: *ISIJ Int.*, 2011, vol. 51, pp. 1724–32.
4. Z.H. Cai, H. Ding, R.D.K. Misra, and Z.Y. Ying: *Acta Mater.*, 2015, vol. 84, pp. 229–36.
5. P.J. Gibbs, E. De Moor, M.J. Merwin, B. Clausen, J.G. Speer, and D.K. Matlock: *Metall. Mater. Trans. A*, 2011, vol. 42, pp. 3691–3702.
6. E. Jimenez-Melero, N.H. van Dijk, L. Zhao, J. Sietsma, S.E. Offerman, J.P. Wright, and S. van der Zwaag: *Acta Mater.*, 2007, vol. 55, pp. 6713–23.
7. Y. Matsuoka, T. Iwasaki, N. Nakada, T. Tsuchiyama, and S. Takaki: *ISIJ Int.*, 2013, vol. 53, pp. 1224–30.
8. I.B. Timokhina, P.D. Hodgson, and E.V. Pereloma: *Metall. Mater. Trans. A*, 2004, vol. 35, pp. 2331–41.
9. R. Blondé, E. Jimenez-Melero, L. Zhao, J.P. Wright, E. Brück, S. van der Zwaag, and N.H. van Dijk: *Acta Mater.*, 2012, vol. 60, pp. 565–77.
10. R. Blondé, E. Jimenez-Melero, R. Huizenga, L. Zhao, J. Wright, E. Bruck, S. van der Zwaag, and N. van Dijk: *Mater. Sci. Eng. A*, 2014, vol. 47, pp. 965–73.
11. H.L. Yi, P. Chen, and H.K.D.H. Bhadeshia: *Metall. Mater. Trans. A*, 2014, vol. 45, pp. 3512–18.
12. H.S. Park, J.C. Han, N.S. Lim, and C.G. Park: *Mater. Sci. Eng. A*, 2015, vol. 627, pp. 262–69.
13. G. Gao, H. Zhang, X. Gui, P. Luo, Z. Tan, and B. Bai: *Acta Mater.*, 2014, vol. 76, pp. 425–33.
14. Y.F. Shen, Y.D. Liu, X. Sun, Y.D. Wang, L. Zuo, and R.D.K. Misra: *Mater. Sci. Eng. A*, 2013, vol. 583, pp. 1–10.
15. X.C. Xiong, B. Chen, M.X. Huang, J.F. Wang, and L. Wang: *Scr. Mater.*, 2013, vol. 68, pp. 321–24.
16. M. Villa, K. Pantleon, and M.A.J. Somers: *J. Alloys Compd.*, 2013, vol. 577, pp. S543–S548.
17. N. Nakada, Y. Ishibashi, T. Tsuchiyama, and S. Takaki: *Acta Mater.*, 2016, vol. 110, pp. 95–102.
18. J. Speer, D.K. Matlock, B.C. De Cooman, and J.G. Schroth: *Acta Mater.*, 2003, vol. 51, pp. 2611–22.
19. A.J. Clarke, J.G. Speer, M.K. Miller, R.E. Hackenberg, D.V. Edmonds, D.K. Matlock, F.C. Rizzo, K.D. Clarke, and E. De Moor: *Acta Mater.*, 2008, vol. 56, pp. 16–22.
20. M. Hillert and J. Ågren: *Scr. Mater.*, 2004, vol. 50, pp. 697–99.
21. J.G. Speer, D.K. Matlock, B.C. DeCooman, and J.G. Schroth: *Scr. Mater.*, 2005, vol. 52, pp. 83–85.
22. M. Hillert and J. Ågren: *Scr. Mater.*, 2005, vol. 52, pp. 87–88.
23. G. a. Thomas, J.G. Speer, and D.K. Matlock: *Metall. Mater. Trans. A*, 2011, vol. 42, pp. 3652–59.
24. S. Kim, J. Lee, F. Barlat, and M.G. Lee: *Acta Mater.*, 2016, vol. 109, pp. 394–404.
25. F. HajyAkbary, J. Sietsma, G. Miyamoto, T. Furuhara, and M.J. Santofimia: *Acta Mater.*, 2016, vol. 104, pp. 72–83.
26. E.J. Seo, L. Cho, and B.C. De Cooman: *Acta Mater.*, 2016, vol. 107, pp. 354–65.
27. Y. Toji, G. Miyamoto, and D. Raabe: *Acta Mater.*, 2015, vol. 86, pp. 137–47.
28. D.T. Pierce, D.R. Coughlin, D.L. Williamson, K.D. Clarke, a J. Clarke, and J.G. Speer: *Acta Mater.*, 2015, vol. 90, pp. 1–14.
29. H. Liu, H. Sun, B. Liu, D. Li, F. Sun, and X. Jin: *Mater. Des.*, 2015, vol. 83, pp. 760–67.
30. M. Karam-Abian, A. Zarei-Hanzaki, H.R. Abedi, and S. Heshmati-Manesh: *Mater. Sci. Eng. A*, 2016, vol. 651, pp. 233–40.

31. Y. Chang, G. Li, C. Wang, X. Li, and H. Dong: *J. Mater. Eng. Perform.*, 2015, vol. 24, pp. 3194–3200.
32. H. Liu, X. Lu, X. Jin, H. Dong, and J. Shi: *Scr. Mater.*, 2011, vol. 64, pp. 749–52.
33. H. Liu, X. Jin, H. Dong, and J. Shi: *Mater. Charact.*, 2011, vol. 62, pp. 223–27.
34. E.A. Ariza, A.S. Nishikawa, H. Goldenstein, and A.P. Tschiptschin: *Mater. Sci. Eng. A*, 2016, vol. 671, pp. 54–69.
35. D. De Knijf, R. Petrov, C. Föjer, and L.A.I. Kestens: *Mater. Sci. Eng. A*, 2014, vol. 615, pp. 107–15.
36. E.J. Seo, L. Cho, and B.C. De Cooman: *Acta Mater.*, 2016, vol. 107, pp. 354–65.
37. G.A. Thomas, F. Danoix, J.G. Speer, S.W. Thompson, and F. Cuvilly: *ISIJ Int.*, 2014, vol. 54, pp. 2900–06.
38. Y. Toji, H. Matsuda, M. Herbig, P.-P. Choi, and D. Raabe: *Acta Mater.*, 2014, vol. 65, pp. 215–28.
39. H. Dong and X. Sun: *Curr. Opin. Solid State Mater. Sci.*, 2005, vol. 9, pp. 269–76.
40. C. Ghosh, V.V. Basabe, J.J. Jonas, Y.M. Kim, I.H. Jung, and S. Yue: *Acta Mater.*, 2013, vol. 61, pp. 2348–62.
41. A. Bardelcik, M.J. Worswick, and M.A. Wells: *Math. Des.*, 2014, vol. 55, pp. 509–25.
42. E.A. Ariza, M. Masoumi, and A.P. Tschiptschin: *Mater. Sci. Eng. A*, 2017, vol. 713, pp. 223–33.
43. K. Thompson, D. Lawrence, D.J. Larson, J.D. Olson, T.F. Kelly, and B. Gorman: *Ultramicroscopy*, 2007, vol. 107, pp. 131–39.
44. G. Thomas, J. Speer, D. Matlock, and J. Michael: *Microsc. Microanal.*, 2011, vol. 17, pp. 368–73.
45. W. Poling, V. Savic, L. Hector, A. Sachdev, X. Hu, A. Devaraj, and F. Abu-Farha: *SAE 2016 World Congress and Exhibition*, 2016. https://doi.org/10.4271/2016-01-0419.
46. D. De Knijf, R. Petrov, C. Föjer, and L.A.I. Kestens: *Mater. Sci. Eng. A*, 2014, vol. 615, pp. 107–15.
47. J. Ågren: *Scr. Metall.*, 1986, vol. 20, pp. 1507–10.
48. A.S. Nishikawa, M.J. Santofimia, J. Sietsma, and H. Goldenstein: *Acta Mater.*, 2018, vol. 142, pp. 142–51.
49. D. De Knijf, R. Petrov, C. Föjer, and L.A.I. Kestens: *Mater. Sci. Eng. A*, 2014, vol. 615, pp. 107–15.
50. M.J. Santofimia, L. Zhao, and J. Sietsma: *Metall. Mater. Trans. A*, 2008, vol. 40, pp. 46–57.
51. I.B. Timokhina, H. Beladi, X.Y. Xiong, Y. Adachi, and P.D. Hodgson: *Acta Mater.*, 2011, vol. 59, pp. 5511–22.
52. I.B. Timokhina, E.V. Pereloma, S.P. Ringer, R.K. Zheng, and P.D. Hodgson: *ISIJ Int.*, 2010, vol. 50, pp. 574–82.
53. B. Hutchinson, J. Hagström, O. Karlsson, D. Lindell, M. Tornberg, F. Lindberg, and M. Thuvander: *Acta Mater.*, 2011, vol. 59, pp. 5845–58.
54. H. Qu: Ph.D. Thesis, Case Western Reserve University, Cleveland, OH, 2013.
55. K. Hase, C. Garcia-Mateo, and H.K.D.H. Bhadeshia: *Mater. Sci. Technol.*, 2004, vol. 20, pp. 1499–1505.
56. H.K.D.H. Bhadeshia: *Bainite in Steels*, 2nd ed., Institute of Materials, London, 2001, pp. 201–24.
57. A. Mohamadizadeh, A. Zarei-Hanzaki, and A. Heshmati-Manesh: *Imandoust. Mater. Sci. Eng. A*, 2014, vol. 607, pp. 621–29.
58. M.J. Santofimia, L. Zhao, and J. Sietsma: *Metall. Mater. Trans. A*, 2008, vol. 40, pp. 46–57.
59. J. Sun and H. Yu: *Mater. Sci. Eng. A*, 2013, vol. 586, pp. 100–7.
60. N. Maheswari, S.G. Chowdhury, K.C.H. Kumar, and S. Sankaran: *Mater. Sci. Eng. A*, 2014, vol. 600, pp. 12–20.
61. E.J. Seo, L. Cho, and B.C. De Cooman: *Metall. Mater. Trans. A Phys. MetallMater. Sci.*, 2014, vol. 45, pp. 4022–37.
62. C. Song, H. Yu, L. Li, T. Zhou, J. Lu, and X. Liu: *Mater. Sci. Eng. A*, 2016, vol. 670, pp. 326–34.
63. J. Dong, X. Zhou, Y. Liu, C. Li, C. Liu, and H. Li: *Mater. Sci. Eng. A*, 2017, vol. 690, pp. 283–93.
64. W. Li, H. Gao, H. Nakashima, S. Hata, and W. Tian: *Int. J. Miner. Metall. Mater.*, 2016, vol. 23, pp. 906–19.
65. W.T. Zhao, X.F. Huang, and W.G. Huang: *Mater. Sci. Technol.*, 2016, vol. 32, pp. 1–8.
66. H.R. Ghazvinloo, A. Honarbakhsh-Raouf, and E. Borhani: *Metallurgist*, 2016, vol. 60, pp. 758–64.
67. M. Gouné, F. Danoix, J. Ågren, Y. Bréchet, C.R. Hutchinson, M. Militzer, G. Purdy, S. van der Zwaag, and H. Zurob: *Mater. Sci. Eng. R Reports*, 2015, vol. 92, pp. 1–38.
68. S. Sun and M. Pugh: *Mater. Sci. Eng. A*, 2000, vol. 276, pp. 167–74.